

Numerical analysis of the influence of magnetic field waveforms on the performance of active magnetic regenerators

Fábio P. Fortkamp · Gusttav B. Lang · Jaime A.
Lozano · Jader R. Barbosa Jr.

Abstract Magnetic cooling is an alternative to vapor compression that does not rely on the use of hazardous substances. The refrigerant is a solid material which reacts to oscillations in magnetic field by changing its temperature (the magnetocaloric effect). In active magnetic regenerators, the magnetocaloric material arranged as a porous medium is subjected to an oscillating fluid flow to allow heat transfer from a cold source to a hot sink in a thermodynamic cooling cycle. Although the literature is abundant with studies on the influence of the fluid flow waveform on magnetic refrigeration devices, the influence of the magnetic field waveform has been much less investigated. In this work, we make use of an active magnetic regenerator numerical model with different mathematically-defined waveforms to determine which operating parameters yield the highest values of cooling capacity and coefficient of

An abridged version of this manuscript was presented at the 24th ABCM International Congress of Mechanical Engineering (COBEM 2017), held in Curitiba, PR, Brazil, in December 2017.

Fábio P. Fortkamp

E-mail: fabio@polo.ufsc.br

Gusttav B. Lang · Jaime A. Lozano · Jader R. Barbosa Jr.

POLO — Research Laboratories for Emerging Technologies in Cooling and Thermophysics, Department of Mechanical Engineering, Federal University of Santa Catarina, Florianópolis, SC, 88040-900, Brazil

performance for a specific set of operating conditions. The results show that the best performance is achieved when the magnetic field is kept constant for the same time duration of the fluid flow through the magnetized material, and that the transition times between the high and low levels of the magnetic field should be as short as possible.

Keywords magnetic refrigeration · active magnetic regenerator · numerical modeling · magnetocaloric effect

List of symbols

Variables

A_t	amplitude of the pressure gradient waveform in the fluid momentum equation [m/s^2]
B	magnetic flux density [T]
c	specific heat [$\text{J}/(\text{kg K})$]
c_E	Ergun constant of the porous medium
COP	coefficient of performance
D_{ld}	dispersion term in the AMR model [m/s^2]
D_p	particle diameter [m]
f	cycle frequency [Hz]
F_B	blow fraction
F_M	magnetization fraction
$g(t)$	dimensional waveform of the pressure gradient term in the fluid momentum equation
\hbar	heat transfer coefficient [$\text{W}/(\text{m}^2 \text{K})$]
H	magnetic field [H]
h	thickness [m]

H_{reg}	regenerator height [m]
K	permeability of the porous medium [m ²]
k	thermal conductivity [W/(mK)]
L_{reg}	regenerator length [m]
\dot{m}_{f}	mass flow rate [kg/s]
M	magnetization field [H]
m	mass [kg]
N_{D}	demagnetization tensor
N_{reg}	number of regenerators
N_{valve}	number of valves
ΔP	total pressure drop across one regenerator [Pa]
P	pressure [Pa]
\dot{Q}_{C}	cooling capacity [W]
\dot{q}_{csg}	volumetric casing losses in the AMR model [W/m ³]
ΔT_{ad}	adiabatic temperature variation [K]
T	temperature [K]
t	time [s]
V	velocity [m/s]
W_{reg}	regenerator width [m]
\dot{W}_{mag}	magnetic power [W]
\dot{W}_{pump}	pumping power [W]
$\dot{W}_{\text{relay},n}$	nominal power consumption of one relay [W]
\dot{W}_{valve}	valve power [W]
$\dot{W}_{\text{valve},n}$	nominal power consumption of one valve [W]
x, y, z	coordinate system variables [m]

Greek symbols

β	surface area density [m^2/m^3]
ε	porosity
Φ	utilization factor
$\eta_{2\text{nd}}$	second-law efficiency
$\tan \theta_{\text{R}}$	ramp rate in the magnetic ramp profile [T/s]
ρ	density [kg/m^3]
τ	time period [s]
$\tau_{0,\text{CC}}, \tau_{0,\text{HC}}$	time periods without fluid flow in the respective half-cycle (see list of Abbreviations) [s]
τ_{B}	blow duration [s]
τ_{M}	magnetization period in the magnetic ramp profile [s]
τ_{R}	ramp period in the magnetic ramp profile [s]
μ_{f}	fluid dynamic viscosity [Pa s]
μ_0	magnetic permeability of free space [H/m]

Subscripts and Superscripts

air	air layer between magnets and regenerators
csg	regenerator casing
eff	effective
f	fluid phase
p	constant-pressure
s	solid phase
sf	relative to the heat transfer between solid and fluid phases in the regenerator
x	yttrium fraction

Abbreviations

AMR	Active Magnetic Regenerator
C	cold source
CB	cold blow
CC	cold cycle
CE	cold end
H	hot source
DoE	design of experiments
HB	hot blow
HC	hot cycle
IT	instantaneous magnetic profile
MCE	Magnetocaloric Effect
MCM	Magnetocaloric Material
MR	Magnetic (or Magnetocaloric) Refrigeration
RC	rectified cosine magnetic profile
RM	ramp magnetic profile

1 Introduction

Although mechanical vapor compression has been the dominant cooling technology for the past century [1], it still faces a number of challenges related to its environmental footprint. For instance, the phase-out of refrigerants with ozone depleting and global warming potentials brought about a more widespread use of flammable substances, which pose a new set of concerns, restrictions and [additional](#) technological challenges for consumer applications [2, 3].

Magnetic refrigeration (MR) is an emerging cooling technology which does not rely on hazardous fluids. In MR, the temperature of a *magnetocaloric material* (MCM) changes as a result of cyclical changes in the applied magnetic field due to the so-called *magnetocaloric effect* (MCE). The magnitude of the MCE depends on material properties, magnetic field variation and temperature, and it is maximum at the Curie temperature of the material [4, 5]. Applications of the MCE at near room-temperature are not restricted to cooling applications [6, 7]; it can also be applied to the development of thermomagnetic motors [8, 9].

For operating temperatures typical of household cooling applications, the MCE is of the order of 2-5 K/T. To amplify this temperature change, heat regeneration is usually employed [5]. Active magnetic regenerators (AMR) are thermal devices in which the magnetocaloric material is packed as a porous matrix subjected to a periodic flow of an aqueous heat transfer fluid. The flow is *synchronized* with successive magnetization and demagnetization steps of the MCM in the porous bed to produce a refrigerating effect. Thus, the AMR is essentially a cascade of infinitesimal “layers” of MCM that are activated simultaneously to build up a longitudinal temperature profile in the matrix. The layers can be made of the same material, resulting in a homogeneous regenerator. However, given the dependence of the MCE on temperature, it is desirable to build *multilayer* regenerators, where each adjacent layer has a slightly different composition that will function around its own Curie temperature, maximizing the magnetocaloric effect of each portion.

A typical AMR cycle is comprised of the following steps: (i) The magnetic circuit magnetizes the MCM, thereby increasing its temperature due to the MCE; (ii) During the *cold blow*, cold fluid previously in thermal contact with the low-temperature source flows through the warm bed, absorbs *part of* its energy and releases it as heat to the high-temperature sink through the hot heat exchanger; (iii) The MCM is demagnetized and cooled down as a result; (iv) As the fluid flow is reversed (*hot blow*), it releases energy to the bed, and decreases

its temperature so it can absorb the thermal load at the cold heat exchanger in contact with the low-temperature source. Different cycles can be devised by changing the duration and synchronization between the two cycle *characteristic waveforms*:

1. The *applied magnetic field profile*, which describes the oscillating magnetic field over one regenerator;
2. The *fluid flow profile*, which describes the time-variation of flow rate through one bed.

Fluid flow profiles can be more easily investigated experimentally, as no changes in the fluid flow hardware are **generally** required, provided **that** a reliable and flexible valving system is in place. In particular, the effect of the *duration* of the fluid blows has been extensively investigated [10, 11, 12]. There appears to be a consensus in the literature that the cooling capacity of magnetic refrigerators can be increased by displacing the fluid during periods where the magnetic field is at its extreme values.

Controlling the duration of the fluid blows can be achieved with the use of solenoid valves; a model for a digital hydraulic system and a calculation of valve power has been presented in Refs. [13, 14]. An application of electronic valves in AMR devices has been presented in Ref. [15], using the control logic (for synchronizing the valve operation with the magnetic profile) described in Ref. [16].

In contrast, because of the complexities involved in designing and fabricating magnetic circuits, the applied magnetic field profiles (or simply the magnetic waveforms) are much less studied, and are usually investigated in **the context** of their synchronization with the fluid flow profile **using** numerical **analysis**. Considering a trapezoidal magnetic profile and a square fluid flow waveform, **one of such analyses** showed that small delays between the increase of the magnetic field and the start of the fluid flow **are** beneficial for the cooling capacity, **as they** assure **that** the solid is fully magnetized before **initiating its energy transfer**

with the fluid [17]. To the authors' knowledge, Ref. [18] was the only work to experimentally vary the magnetic profile, by controlling the rotation of magnetic cylinders. They also showed that the cooling capacity of an AMR device depends on the time lag between magnetization and fluid flow.

If the time delay between magnetization and fluid displacement is further increased so that the fluid flow period can coincide with different stages of the magnetic profile, different thermodynamic cycles can be obtained with different performance trends; the Brayton AMR cycle (explained previously) yields the highest cooling capacities, while the Ericsson AMR cycle — with isothermal (de)magnetization steps — yields the highest values of the coefficient of performance [19]. This conclusion was confirmed by a more extensive numerical analysis in Ref. [5], which also varied the amplitude of the trapezoidal magnetic profile and proposed magnetic circuit designs capable of generating such profiles. Ref. [20] carried out a numerical comparison of the square wave (step change), sinusoidal and rectified cosine magnetic profiles for a sinusoidal fluid profile and concluded that the cooling capacity and maximum temperature spans are maximal for the instantaneous magnetic profile.

As previously noted, the fluid flow profile is implemented with a proper design of the fluid flow system, while the magnetic profile is an important input when designing a magnetic circuit [21]. With the goal of AMR design in mind, none of the works revised in this paper considered different *shapes* and *amplitudes* of the magnetic field waveform. Regarding shape, the combination of a trapezoidal magnetic profile and an instantaneous fluid flow profile currently prevails in the literature [17, 18, 22], and this is also the situation investigated in the present paper. However, sinusoidal magnetic profiles can be achieved with more compact systems [23], and their generation and impact on AMR performance have been investigated in our group [24, 25]. However, no work has investigated how these waveforms, when synchronized with optimized fluid flow profiles, measure up against the instantaneous

magnetic profile, which is recognised in the literature as the optimal waveform for when the fluid flow profile is fixed.

As far as the incorporation of the magnetic field waveform in the AMR performance optimization is concerned, the studies published in the open literature can be classified into three categories, namely *segregated*, *semi-segregated* and *integrated* design. In the first category, the magnetic field waveform remains constant (i.e., fixed shape and amplitude) during the AMR optimization. In the semi-segregated approach, parameters associated with the magnetic field waveform are allowed to change, but no consideration is given to the configuration of the magnetic circuit (i.e., magnet materials, geometry, segmentation) needed to generate such waveforms. Finally, in the integrated design approach, the magnetic circuit that generates the waveform is mathematically incorporated in the analysis (through conservation equations and appropriate closure relationships involving the magnetic field), so objective functions may now be formulated involving the mass, size, geometry or material cost of the magnetic circuit. Refs. [26, 27] are examples of segregated AMR optimization. In Ref. [26], single-objective optimization coupled with a dimensionless parametric analysis enabled identifying the utilization factor that optimized the performance of Gd-based AMRs in terms of the temperature span and cooling capacity. Ref. [27] introduced a detailed numerical model of a sixteen-layer La-Fe-Mn-Si-H parallel-plate AMR, and coupled it with a DoE-based (Design of Experiment) optimization method. A square wave magnetic field waveform with a 1.5-T maximum magnetic flux density was applied. Examples of semi-segregated AMR optimization are given in Refs. [28, 29, 30], where multi-objective optimization techniques were employed to optimize the performance of parallel-plate [30] and sphere packed-bed AMRs [29] using methods such as weighted sum, weighted product and genetic algorithms, among others. A common finding to all of such studies is that no configuration exists which can simultaneously optimize all objectives (e.g., cooling ca-

capacity and temperature span), so a compromise is required according to specified design constraints. Finally, in their *integrated* approach to AMR optimization, Ref. [31] employed a topology-based optimization of the magnetic circuit (using genetic algorithms) to reduce to a minimum the cost of cooling. In this sense, not only the capital costs were considered (using simple prismatic magnet segments in the magnetic circuit), but also the operating costs associated with the AMR itself. More recently, in Ref. [25], a magnetic circuit consisting of concentric Halbach cylinders was analytically modelled and integrated with models for the power expenditure of the flow management system and for the fluid flow and heat transfer in the AMR to determine the geometric characteristics of the latter which maximized its performance. Designer maps, which embodied the existing trade-offs between the system variables, provided easy visual access to the regenerator dimensions which maximized the cooling capacity or the COP.

The present work *complements* the previously mentioned studies by investigating the performance of a magnetic refrigerator *subjected to* different magnetic profile waveforms. The cooling capacity and *the COP* are calculated *taking account of the magnetic profile* parameters, while also *considering* how the AMR geometry affects the performance *parameters in conjunction* with the magnetic profile. *To simplify the analysis*, the *shape of the* fluid flow *waveform* is assumed fixed, *but some of* its parameters are also varied. To emulate constraints on an operating point of actual magnetic refrigeration devices, the temperature span is kept fixed, so a few comments are made *regarding the* second-law efficiency.

2 Materials and methods

As explained *before*, we performed numerical simulations using a previously developed AMR model, varying the profile-specific and geometric parameters. We also implemented a

model to calculate the power consumption of a novel fluid management system, which is a topic not yet extensively studied in the literature. The output variables from this integrated model are the cooling capacity, the several power contributions (the magnetic power to magnetize the material, the pumping power to overcome pressure drop in the regenerator, and the power to actuate the electronic valves) and the coefficient of performance (COP).

2.1 AMR model

2.1.1 Governing equations

Simulations were performed using a one-dimensional AMR mathematical model, implemented using the Finite Volume Method [32]. The model solves momentum and energy balance equations for the solid and fluid phases, represented by indices 's' and 'f', respectively. The model geometry is shown in Figure 1, and assumes that the regenerator is composed of monodisperse packed spheres with porosity ε .

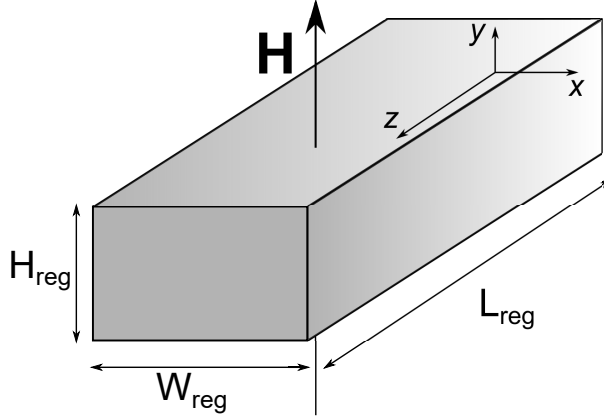


Fig. 1: AMR model geometry

The momentum equation for the fluid domain is given by:

$$\frac{\rho_f}{\varepsilon} \frac{\partial V_z}{\partial t} = -\frac{\partial P}{\partial z} - \frac{\mu_f}{K} V_z - \frac{c_E \rho_f}{K^{1/2}} |V_z| V_z \quad (1)$$

where the macroscopic inertial term on the left-hand side is balanced with the pressure gradient, Darcy stress and Forchheimer drag [33]. The momentum equation is solved for the time-dependent uniform fluid velocity V_z through the bed.

The energy equation for the fluid phase can be written as:

$$\begin{aligned} \rho_f c_{p,f} \left(\varepsilon \frac{\partial T_f}{\partial t} + V_z \frac{\partial T_f}{\partial z} \right) = & -\hbar_{sf} \beta (T_f - T_s) \\ & + \left| V_z \frac{\partial P}{\partial z} \right|_f \\ & + \varepsilon \left(k_f^{\text{eff}} + \rho_f c_{p,f} D_{ld} \right) \frac{\partial^2 T_f}{\partial z^2} \\ & + \dot{q}_{csg} \end{aligned} \quad (2)$$

where the left-hand side includes the inertial and advection terms, and the right-hand side includes terms for the solid-fluid heat transfer, viscous dissipation, heat conduction, porous-media dispersion, and casing losses.

The energy equation for the solid phase is written as:

$$\rho_s c_s (1 - \varepsilon) \frac{\partial T_s}{\partial t} = \hbar_{sf} \beta (T_f - T_s) + (1 - \varepsilon) k_s^{\text{eff}} \frac{\partial^2 T_s}{\partial z^2} \quad (3)$$

where the terms represent respectively inertia, solid-fluid heat transfer and heat conduction.

Initial and boundary conditions, closure relations for the porous media terms, solution methods and convergence criteria and analyses are discussed in detail in [32]. This AMR model solves the above equations for one regenerator operating between given source temperatures (assuming ideal heat exchangers in contact with the thermal reservoirs), during one full cycle (hot and cold blows and magnetization and demagnetization periods), given specified operating conditions (to be discussed later).

The casing heat transfer term \dot{q}_{csg} in Equation 2 is calculated solving the heat conduction equation in the regenerator casing [32]. It can be neglected in some circumstances if an insulating casing material is assumed, which greatly simplifies the analysis.

2.1.2 Fluid flow profile modeling

The pressure gradient in Equation 1 is modeled as:

$$-\frac{\partial P}{\partial z} = \rho_f A_t g(t) \quad (4)$$

where $g(t)$ is a dimensionless function that expresses the mathematical waveform of the pressure gradient, and A_t is its amplitude, adjusted in a convergence loop. In this loop, the mass flow rate calculated in terms of the Darcy velocity from Equation 1 is compared with the input mass flow rate until convergence is obtained.

The canonical fluid flow profile considered in this work is the square wave or *instantaneous profile*, because of the instantaneous change in flow rate, as shown in Figure 2.

The instantaneous mass flow rate, $\dot{m}_f(t)$, is defined over a cycle with a period τ , and represents the fluid flow through a given regenerator bed. The so-called *hot cycle*, during which the MCM is magnetized, occupies the time interval $0 \leq t < \tau/2$, while the *cold cycle* lies between $\tau/2 \leq t \leq \tau$. The flow profile oscillates between two plateaus of equal magnitude $\dot{m}_{f,\text{max}}$ and opposite directions, which are centered in each half-cycle. During the hot cycle, the cold blow period is τ_{CB} , and during the cold cycle the hot blow period is τ_{HB} . If balanced flow exists, then $\tau_{\text{CB}} = \tau_{\text{HB}}$.

During each half cycle, there are periods without fluid flow defined as:

$$\tau_{0,\text{HC}} = \frac{\tau/2 - \tau_{\text{CB}}}{2} \quad (5)$$

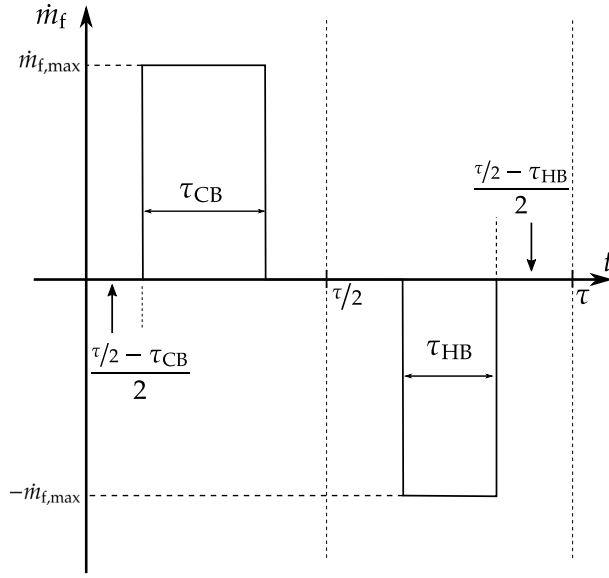


Fig. 2: Instantaneous fluid flow profile. Adapted from [25].

$$\tau_{0,CC} = \frac{\tau/2 - \tau_{HB}}{2} \quad (6)$$

where HC and CC stand for hot cycle and cold cycle, respectively.

The [fluid flow](#) profile can be mathematically defined as:

$$\dot{m}_f(t) = \begin{cases} 0, & 0 \leq t < \tau_{0,HC} \\ \dot{m}_{f,max}, & \tau_{0,HC} \leq t \leq \tau/2 - \tau_{0,HC} \\ 0, & \tau/2 - \tau_{0,HC} < t < \tau/2 + \tau_{0,CC} \\ -\dot{m}_{f,max}, & \tau/2 + \tau_{0,CC} \leq t \leq \tau - \tau_{0,CC} \\ 0, & \tau - \tau_{0,CC} < t < \tau \end{cases} \quad (7)$$

When the blows have different time durations, the AMR cycle is considered unbalanced, and that is known to have a negative effect on performance [11, 34]. In this work, the blows

are always balanced, hence the blow fraction, i.e., the ratio of blow durations to cycle period [11], can be evaluated as:

$$F_B = \frac{2\tau_B}{\tau} \quad (8)$$

where τ_B is the duration of one blow.

2.1.3 Magnetic profile modeling

The magnetic profile is modeled by a waveform of magnetic field strength, $H(t)$, applied perpendicular to the regenerators, as shown in Figure 1. The magnetic field is assumed uniform throughout the beds. The applied field is corrected from demagnetization effects to yield the effective field inside the regenerators:

$$H^{\text{eff}} = H - N_D M \quad (9)$$

where M is the magnetization field of the material, and N_D is a demagnetization factor.

The magnetocaloric effect is implemented using the so-called discrete approach [35]; every time the magnetic field changes, based on the input magnetic profile, the solid temperature is calculated according to:

$$T_s(t + \Delta t) = T_s(t) + \Delta T_{\text{ad}} \left(T_s(t), H^{\text{eff}}(t), H^{\text{eff}}(t + \Delta t) \right) \quad (10)$$

where the adiabatic temperature variation, ΔT_{ad} , a standard measure of the MCE, is calculated from tabulated experimental data for magnetocaloric materials as function of temperature and effective field [32]. [Experimental curves for \$\Delta T_{\text{ad}}\$ as a function of temperature and magnetic field change can be found in Ref. \[36\].](#)

The magnetic profiles considered in this work are presented in terms of the flux density $B = \mu_0 H$, where μ_0 is the permeability of free space; the magnetic field H is used in the evaluation of the magnetocaloric effect.

The instantaneous (square wave) profile (represented by the subscript “IT”) and the rectified cosine profile (represented by “RC”) are defined solely in terms of the extreme values B_{\min} and B_{\max} , and are shown in Figure 3.

$$B_{\text{IT}}(t) = \begin{cases} B_{\max}, & 0 \leq t < \tau/2 \\ B_{\min}, & \tau/2 \leq t < \tau \end{cases} \quad (11)$$

$$B_{\text{RC}}(t) = B_{\min} + (B_{\max} - B_{\min}) \left| \cos \left(\frac{\pi}{\tau} \left(t - \frac{\tau}{4} \right) \right) \right| \quad (12)$$

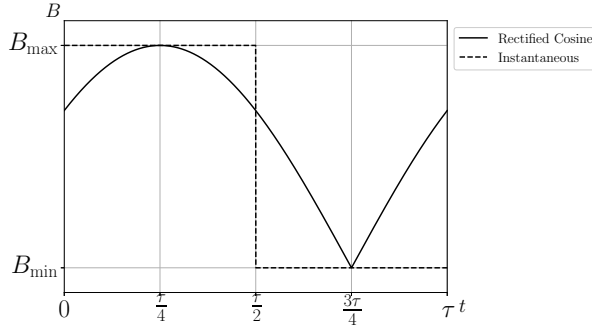


Fig. 3: Instantaneous ("IT") and rectified cosine ("RC") magnetic profiles

A suitable approximation of the instantaneous profile is the *magnetic ramp profile*, shown in Figure 4, with finite transition times between the levels of constant magnetization. The magnetic profile oscillates between a low value B_{\min} and a high value B_{\max} , and remains at each plateau for a period of τ_M . The plateaus are balanced and centered at each half-cycle.

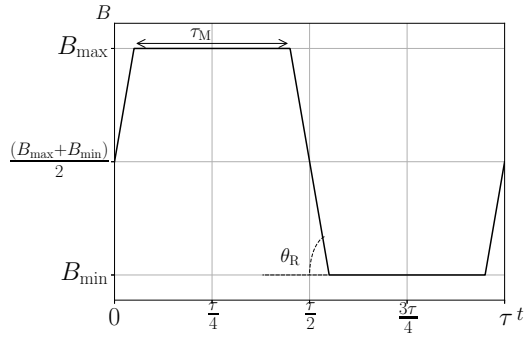


Fig. 4: Magnetic ramp profile

The *ramp period* τ_R is defined as:

$$\tau_R = \frac{1}{4} (\tau - 2\tau_M) \quad (13)$$

such that there are four ramp periods in one full cycle. The ramp rate, $\tan \theta_R$, is [given by](#):

$$\tan \theta_R = \frac{(B_{\max} - B_{\min})}{2\tau_R} \quad (14)$$

The magnetization fraction, F_M , is the fraction of the cycle during which the magnetocaloric material is subjected to a constant magnetic field:

$$F_M = \frac{2\tau_M}{\tau} \quad (15)$$

The ramp profile (“RM”) can be mathematically defined as:

$$B_{RM}(t) = \begin{cases} (B_{\max} + B_{\min})/2 + t \tan \theta_R, & 0 \leq t < \tau_R \\ B_{\max}, & \tau_R \leq t < \tau/2 - \tau_R \\ B_{\max} - (t - (\tau/2 - \tau_R)) \tan \theta_R, & \tau/2 - \tau_R \leq t < \tau/2 + \tau_R \\ B_{\min}, & \tau/2 + \tau_R \leq t < \tau - \tau_R \\ B_{\min} + (t - (\tau - \tau_R)) \tan \theta_R, & \tau - \tau_R \leq t \leq \tau \end{cases} \quad (16)$$

Additionally, the average values of the magnetic field during each half-AMR cycle are considered for comparison between profiles. The average magnetic profile during the hot cycle ($0 \leq t < \tau/2$) is denoted by \bar{B}_{high} and the average during the cold cycle ($\tau/2 \leq t < \tau$) is denoted by \bar{B}_{low} . For the instantaneous waveform, these average values are identical to the extreme values.

2.1.4 Evaluation of solid and fluid properties

The fluid properties are considered constant in the momentum equation to decouple the solution procedures to determine the velocity and temperature fields. The properties are computed at the average temperature between the hot and cold sources, and are evaluated from interpolation of tables imported from the EES software [37]. In all simulations shown in this work, the heat transfer fluid is a 80/20 vol.% mixture of water/ethylene-glycol. For the energy equations, the fluid properties are also calculated from tabulated data, but the temperature dependence is considered.

Both single- and multilayer regenerators are considered in this study. Single-layer regenerators are composed of gadolinium, a benchmark material with a Curie temperature of 290 K. For simplicity, the solid density is assumed constant at $\rho_s = 7900 \text{ kg/m}^3$ and the solid thermal conductivity is set to $k_s = 10.5 \text{ W/(mK)}$. The specific heat capacity of Gd is

calculated as a function of temperature and magnetic field based on experimental data, using a bi-linear interpolation scheme; more details on the experimental dataset are available in [32].

For the multilayer simulations, gadolinium-yttrium alloys are used, $\text{Gd}_{1-x}\text{Y}_x$, where x is the yttrium fraction. This fraction reduces the Curie temperature of the alloy relative to that of pure gadolinium. Due to the lack of experimental data on the magnetocaloric properties of $\text{Gd}_{1-x}\text{Y}_x$ alloys at the time this analysis was made, a simpler approach was used in which the dependence of magnetization, specific heat capacity and entropy with respect to the magnetic field for alloys with a low yttrium fraction are identical to those of pure gadolinium, but are shifted to a lower Curie temperature (corresponding to the yttrium fraction).

2.1.5 Performance metrics

The AMR model is solved for only one bed, but assumes that the N_{reg} identical beds experience the same cycle. Thus, the extensive performance parameters are multiplied by that factor. The cooling capacity is calculated as [32]:

$$\dot{Q}_C = N_{\text{reg}} \frac{1}{\tau} \int_{\tau_{\text{HB}}} \dot{m}_f(t) c_{p,f} (T_C - T_{f,\text{CE}}) dt \quad (17)$$

As pointed out in Ref. [25], since external sources of irreversibility (e.g., heat transfer with a finite temperature difference in the heat exchangers) are ignored and no eddy currents and hysteresis losses are present, the magnetic power required to magnetize the solid refrigerant and produce the MCE in the AMR cycle is given by the product of the Carnot efficiency and the cooling capacity as follows:

$$\dot{W}_{\text{mag}} = \dot{Q}_C \frac{T_H - T_C}{T_C} \quad (18)$$

Irreversibility due to fluid friction is accounted for in the calculation of the pumping power:

$$\dot{W}_{\text{pump}} = N_{\text{reg}} \frac{1}{\tau} \int_0^\tau \frac{\dot{m}_f}{\rho_f} \Delta P dt \quad (19)$$

where ΔP is the total pressure drop through the regenerator (including one hot and one cold blow).

2.2 Hydraulic system and fluid flow profile model

The hydraulic system designed to modulate the fluid flow through different regenerators at different time instants is composed of a pump and a set of electronic valves which can be precisely controlled to yield the desired blow durations. The electrical power consumed by the valve array is computed separately from other work contributions.

In the present analysis, two types of valves are considered. In the first approach, called *Type R valves*, the model proposed in Ref. [13] is used, assuming that the individual power consumption of each valve is independent of frequency and blow fraction. The valve power, \dot{W}_{valve} , can be computed as:

$$\dot{W}_{\text{valve}} = N_{\text{valve}} F_B \left(\dot{W}_{\text{valve},n} + \frac{1}{2} \dot{W}_{\text{relay},n} \right) \quad (20)$$

where N_{valve} is the number of valves, $\dot{W}_{\text{valve},n}$ is the measured average nominal power for one normally-closed electronic valve and $\dot{W}_{\text{relay},n}$ is the nominal power for one controlling relay. The factor $1/2$ is due to two valves being controlled by one relay.

In the second approach, *Type S* valves are used, which have a nominal power lower in magnitude, but which depends on the frequency and blow fraction. These valves were experimentally characterized in Ref. [14], where a single valve was attached to a measurement circuit and set to operate for a range of values of blow fraction and frequency; the valve power was calculated from the averaged values of voltage and current after the periodic steady state was reached. From those experiments, the valve power was experimentally correlated as:

$$\dot{W}_{\text{valve}} [\text{W}] = N_{\text{valve}} (0.927f [\text{Hz}] + 1.023F_{\text{B}} + 0.226f [\text{Hz}]F_{\text{B}} - 0.037) \quad (21)$$

Equation (21) was correlated for blow fractions of 50 and 100 % and frequencies in the range of 0.2–1.6 Hz, with an uncertainty on the order of 0.4 W for a single valve. The use of different valve types will be discussed in the Results section.

Independent of the valve type used, it is also assumed that each valve system is capable of producing the fluid flow profile shown in Figure 2, where the displaced fluid mass during one blow in one regenerator bed is $\dot{m}_{\text{f,max}} F_{\text{B}} \tau / 2$. The utilization factor can then be calculated as:

$$\Phi = \frac{\dot{m}_{\text{f,max}} F_{\text{B}} c_{p,\text{f}}}{2f m_{\text{s}} c_{\text{s}}} \quad (22)$$

and in all results shown in this work, the number of valves is calculated as:

$$N_{\text{valve}} = 2N_{\text{reg}} \quad (23)$$

2.3 Coefficient of performance and second-law efficiency

The coefficient of performance is calculated as the ratio of the cooling capacity — the main output parameter from the AMR model — and all previously cited power contributions:

$$\text{COP} = \frac{\dot{Q}_C}{\dot{W}_{\text{pump}} + \dot{W}_{\text{mag}} + \dot{W}_{\text{valve}}} \quad (24)$$

The maximum possible COP between the source temperatures is the Carnot COP, calculated as:

$$\text{COP}_{\text{Carnot}} = \frac{T_C}{T_H - T_C} \quad (25)$$

and the second-law efficiency is defined as:

$$\eta_{2\text{nd}} = \frac{\text{COP}}{\text{COP}_{\text{Carnot}}} \quad (26)$$

3 Results and Discussions

The analysis of the magnetic profiles was performed at two different stages. Initially, the instantaneous (square-wave) and the rectified cosine profiles are compared using a simpler approach (i.e., neglecting casing losses). Later, based on the selection of the most promising magnetic profile, a more in-depth analysis was carried out to determine the optimal geometric and operating parameters of the AMR system.

3.1 Comparison of instantaneous and rectified cosine profiles using a simplified model

At the first stage of the present analysis, the instantaneous and rectified cosine profiles are compared considering a single-layer regenerator without casing losses, using Type R valves. The parameters used in all simulations are presented in Table 1.

Table 1: AMR parameters kept fixed in the simulations with different magnetic profiles

Parameter	Value
D_p	0.5 mm
H_{reg}	20 mm
W_{reg}	25 mm
L_{reg}	100 mm
N_{reg}	11
N_{valve}	22
T_H	298 K
T_C	278 K
$\dot{W}_{\text{valve},n}$	4 W
$\dot{W}_{\text{relay},n}$	0.36 W

When comparing the performances resulting from the application of the different magnetic profiles, the same average magnetic field during the hot cycle will be considered; this implies a higher peak for the rectified cosine. For the cold cycle, the minimum values for both profiles are the same, as shown in Figure 5. As a reference, in all simulations, the minimum value for the rectified cosine was fixed at $B_{\text{min}} = 0.1$ T.

Simulations were carried out for various values of blow fraction. The rectified cosine profile can benefit from smaller blow fractions that concentrate the flow during the periods of very high and very low fields, thereby increasing the average variation in magnetic field [11];

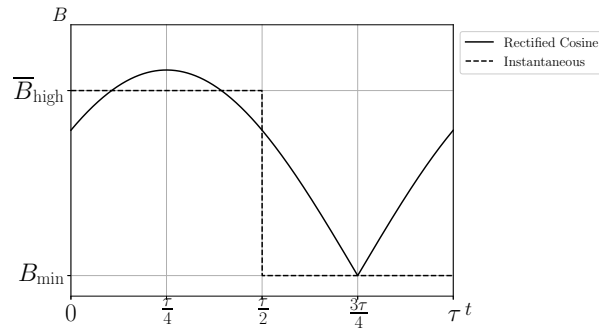


Fig. 5: Configuration of average and extreme values of the instantaneous and rectified cosine profiles

this is not observed with the instantaneous profile, since the field is constant and reducing the blow fraction will only reduce the period when the fluid is in contact with the warm solid, decreasing the regenerator effectiveness. In this section, all results use the critical value of blow fraction that maximized the cooling capacity: fluid flowing during the entire period for the instantaneous profile, and only during 60 % of the period (the smallest blow fraction tested) for the cosine profile; this latter case is shown in Figure 6.

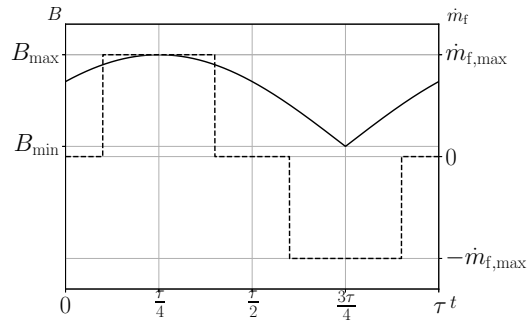


Fig. 6: Rectified cosine magnetic profile (solid lines) and the instantaneous flow profile with blow fraction of 60 % (dashed lines)

Figure 7 shows the cooling capacity attained by the device at a frequency of 1 Hz for different utilizations. The horizontal axis shows the average field value during the high field region. The instantaneous profile almost always yields a higher performance, and since the average field during the hot cycle (high field stage) is the same, the main difference is due to the low magnetic field levels. In this comparison, the instantaneous profile is capable of keeping a low magnetic field over the entire half-cycle, which is beneficial for performance; as demonstrated in Ref. [20], a higher average magnetic field during the low-field stage increases the solid temperature and consequently results in warmer fluid entering the cold heat exchanger, representing a thermal loss. Analyzing points of different profiles of constant utilization (which should result in the same regenerator effectiveness), for $\Phi = 1.0$ and $B_{\text{high}} = 1.40 \text{ T}$, the cooling capacity for the instantaneous profile is 196.3% higher than for the cosine profile. This results from the fluid being able to cool down to lower temperatures during the low-field cycle, since the cosine profile cannot maintain the field as low as the instantaneous profile (cf. Figure 5), even with the reduction of blow fraction.

The only exception in this comparison is observed for the lowest utilization of $\Phi = 0.2$, where the performance is slightly better for the RC profile. Since the blow fraction for the cosine is smaller, the mass flow rate is higher in the latter for the same utilization (cf. Eq. (12)). This increases the heat transfer rate, as previously explained — outweighing the effects of the magnetic field.

Also noticeable in Figure 7 is the non-linear relationship between cooling capacity and utilization. For instance, for the “RC” profile at the highest magnetic field, the cooling capacity increases when the utilization is raised from 0.2 to 0.6, but then returns to the same levels with a further increase of the utilization to 1.0. Since the frequency is constant in Figure 7, increasing the utilization means increasing the mass flow rate; initially, this results in higher heat transfer rates due to higher Nusselt numbers, but further increase reduces the

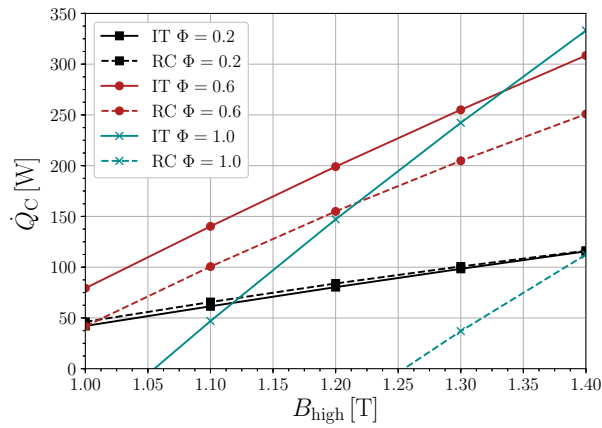


Fig. 7: Cooling capacity as a function of the average high magnetic field, for different utilizations. “IT”: instantaneous (blow fraction of 100 %); “RC”: rectified cosine (blow fraction of 60 %).

effectiveness and amplifies viscous dissipation, to the point where the cooling capacity is null for certain points with the highest utilization.

The same analysis, but in terms of the coefficient of performance, is shown in Figure 8, where the instantaneous profile yields better results for medium to high levels of utilization. This can be explained based on the behavior of the magnetic, valve and pumping powers shown in Figure 9 for a fixed utilization of 0.6. As can be seen, the magnetic power only differs between the profiles due to changes in cooling capacity. Also, the valve power is higher for the instantaneous profile since the valves must remain open for longer periods. However, the proportional increase in pumping power, due to larger flow rates when operating with the smaller blow fraction of the “RC” profile, is even higher (than the change in valve power). Although not shown in Figure 9, the effect of higher utilization levels is to make the pumping power even more relevant; as depicted in Figure 8, the lowest levels of

the coefficient of performance are attained with the smallest blow fraction (for the rectified cosine profile) and higher utilization, corresponding to the highest flow rate levels.

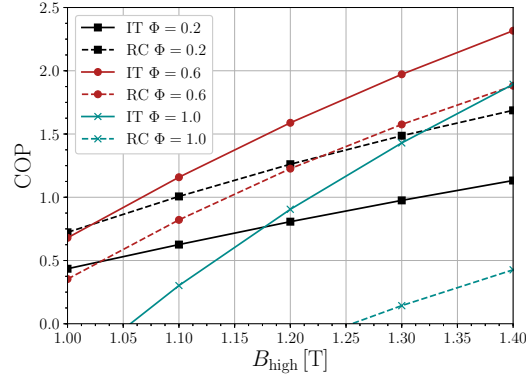


Fig. 8: Coefficient of performance as a function of the average high magnetic field, for different values of utilization. “IT”: instantaneous (blow fraction of 100 %); “RC”: rectified cosine (blow fraction of 60 %).

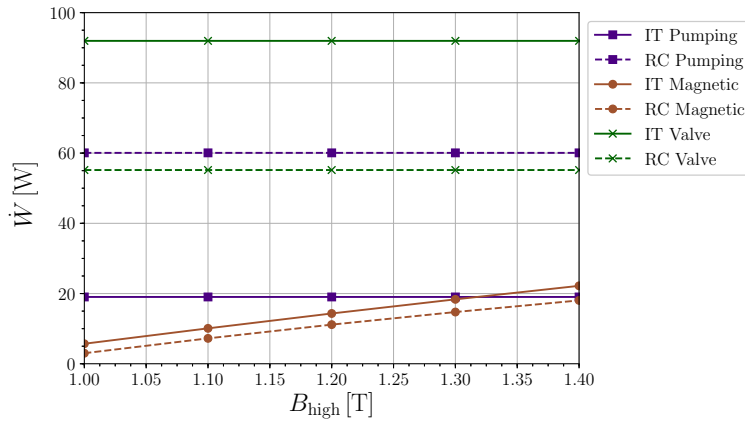


Fig. 9: Power contributions as a function of the average high magnetic field, for a utilization of 0.6. “IT”: instantaneous (blow fraction of 100 %); “RC”: rectified cosine (blow fraction of 60 %).

In general, considering target values for the cooling capacity, AMRs operating with the instantaneous magnetic profile lead to better performance results. As can be seen in Fig. 7, an instantaneous profile with the lowest possible value of B_{\min} and the highest possible value of B_{\max} , with a flow profile occupying the whole cycle with average values of utilization, results in the highest values of cooling capacity among all simulations.

The rectified cosine profile, found in compact systems using Halbach arrays, can surely benefit from reducing the blow fraction, both in terms of cooling capacity and temperature span. However, for the typical parameters evaluated in this paper, even if the blow fraction is optimized for the “RC” profile, the “IT” profile still gives better results.

3.1.1 Analysis of the instantaneous profile

As shown in the previous section, the instantaneous profile generally yields the highest values of cooling capacity. Therefore, in this section, a more detailed analysis of this profile is carried out, where the maximum field is varied, but the minimum value is kept at 0.05 T. Figure 10 shows the cooling capacity as a function of the utilization, for several levels of the maximum magnetic field and two different operating frequencies. Because of the conflict between a low heat transfer rate for flow rates that are too low and losses in regenerator effectiveness in flow rates that are too high, there are critical values of utilization that maximize the cooling capacity, and these critical values increase with the magnetic field. For higher magnetic fields, the increase in the MCE surpasses the loss of effectiveness, and one can go to higher flow rates without losing performance. It can also be seen in Fig. 10 that at higher frequencies the values of cooling capacity are higher, and also the critical values of utilization are lower. However, this is usually achieved at the expense of [an even](#) higher power consumption at higher frequencies [38, 39], resulting in a decrease of the coefficient of performance with frequency. [Critical values of utilization that maximize the COP](#)

(all other parameters fixed) are also observed, but these tend to be smaller than the critical values for cooling capacity; at higher utilization levels, the pumping power increases more rapidly than the cooling capacity.

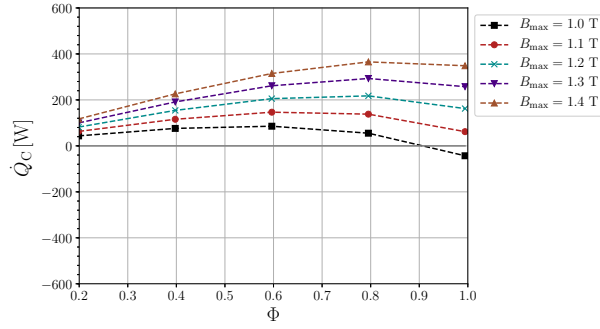
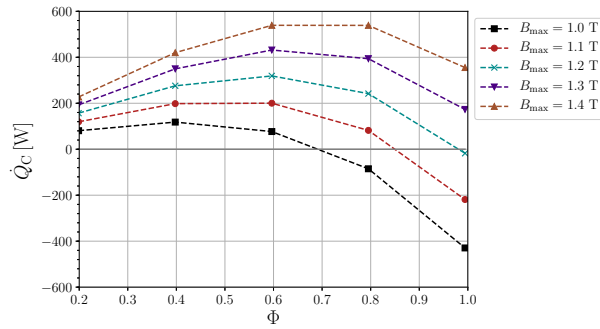
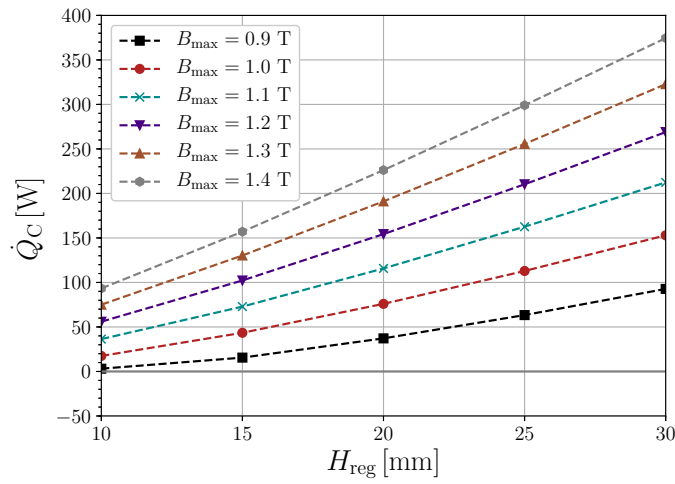
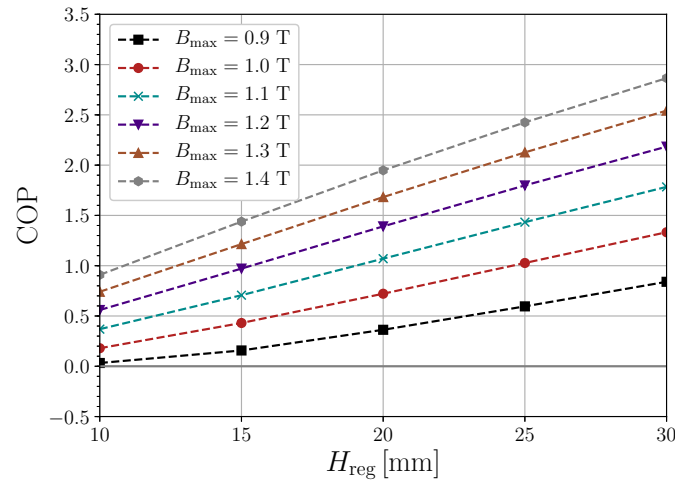
(a) $f = 1$ Hz(b) $f = 2$ Hz

Fig. 10: Cooling capacity as a function of utilization, for various values of the high magnetic field for the instantaneous profile

The geometric parameters in Table 1 were chosen from preliminary simulations, so they are not optimal. To understand the impact of the regenerator geometry on the system performance with the instantaneous profile, the regenerator height was varied in Fig. 11, and all other parameters from Table 1 were kept fixed and with $\phi = 0.4$. The height was chosen as



(a) Cooling capacity



(b) Coefficient of performance

Fig. 11: Performance metrics as a function of the regenerator height (all other parameters were set as in Table 1, for utilization factor of 0.4) for various values of the high magnetic field of the instantaneous profile

the geometric parameter to be varied as it usually represents a design trade-off in magnetic

refrigerators [25]: taller regenerator cross-sections allow for more magnetocaloric material while reducing the volume of the magnetic circuit (cf. Figure 12).

As expected, higher magnetic fields allow for smaller regenerators (hence more compact systems) to achieve a desired cooling capacity. For instance, to achieve a capacity of 100 W, increasing the field from 1.0 to 1.2 T results in regenerators that are 36 % smaller. Comparing the results for the cooling capacity and coefficient of performance, the trends are largely the same, as the former is more sensitive to variations in the magnetic field and regenerator height than the components of power; note that increasing the regenerator height increases the mass of magnetocaloric material, hence increasing the cooling capacity, but it also changes the area available for the fluid flow (influencing pumping power) and the demagnetization factor (influencing the magnetic power).

3.2 In-depth analysis of the magnetic ramp profile

Based on the better performance of the instantaneous profile, the ramp profile is a naturally suitable target profile for the design of magnetic refrigerators, and will be analyzed in this section, representing the second stage in the analysis of magnetic profiles.

Moving towards a more realistic model, casing losses are included, using the model from Ref. [32]. The bed is enclosed in a solid casing of thickness h_{csg} , and two air layers of thickness h_{air} separate the AMR and its casing from the inner and outer magnet cylinders, as shown in Figure 12. The optimal design of such magnetic cylinders aiming at a particular magnetic profile will be the subject of future publications.

Preliminary analyses carried out in Ref. [40] showed that a stainless steel casing with a thickness of $h_{\text{csg}} = 0.5 \text{ mm}$ is thick enough to ensure mechanical integrity and easy manu-

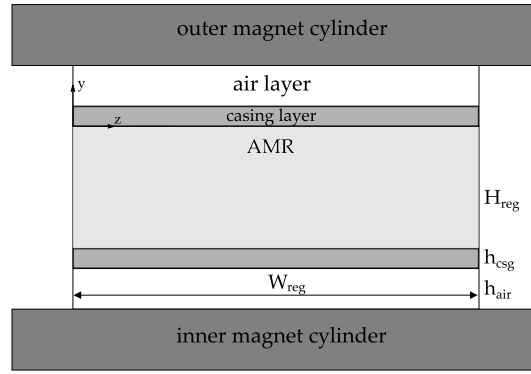


Fig. 12: Model for the casing losses in regenerators

facturing, while being thin enough to accommodate the material with a low thermal conductivity.

In addition, in the present study, an air gap clearance thickness was set at $h_{air} = 1$ mm. This value gave rise to a peak in cooling capacity due to the compromise between minimizing losses and maximizing the magnetocaloric mass. The thermophysical properties of stainless steel and air were also obtained with interpolation of tables exported by the EES software [37].

The simulations in this section also use multilayer regenerators. A summary of all parameters adopted in this section, including the Curie temperatures and volumetric fractions (relative to the length of the bed) of each layer is presented in Table 2; more details on the selection of these parameters are shown in Ref. [41]. In addition, in the following results, Type S valves are used, with valve power calculated by Equation 21.

Figure 13 shows the two profiles that will be used in this section and how they are synchronized. Regarding the magnetic profile, the magnitude of the high value will be varied to investigate the performance of the AMR system, while the minimum will be kept **fixed** at $B_{min} = 0.05$ T.

Parameter	Value
W_{reg}	30 mm
L_{reg}	85 mm
N_{reg}	8
N_{valve}	16
f	1 Hz
T_{H}	305.5 K = 32.5 °C
T_{C}	270.5 K = -2.5 °C
D_{p}	350 μm
h_{csg}	0.5 mm
h_{air}	1 mm
Casing material	Stainless steel
Number of layers	3
Curie temperatures of each layer	273, 283, 290 K
Length fractions of each layer	20, 20, 60 %

Table 2: Fixed parameters for the AMR simulations used in this chapter

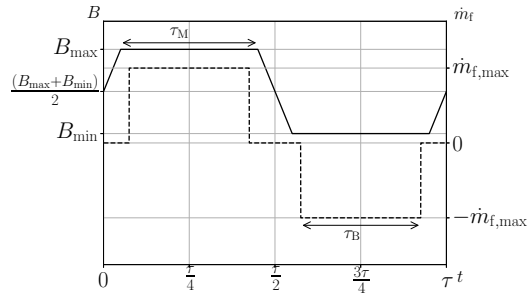


Fig. 13: Comparison between the magnetic ramp profile (solid line) and the instantaneous fluid flow profile (dashed line)

3.2.1 Performance curves for variable blow and magnetization fractions

Figure 14 shows the cooling capacity and coefficient of performance of the AMR system for a fixed utilization factor of 0.4 and for a magnetic profile with a maximum at 1.3 T, for variable blow and magnetization fractions. To facilitate the analysis, the results are plotted in terms of the ratio F_M/F_B , with curves for different values of F_B . It is clear that both the cooling capacity and the coefficient of performance exhibit a peak at $F_M = F_B$. Moreover, to the right of the peak, i.e., for higher values of F_M , the reduction of both performance metrics is slower, meaning it is better to have a magnetization plateau that is wider than the fluid flow plateau.

The reduction in performance for $F_M > F_B$ can be explained by an increase in heat leakage through the casing, as the solid begins to lose energy to the environment when the fluid is not flowing. For $F_M < F_B$, the fluid begins to flow when the solid is not totally warmed up, losing effectiveness, and this effect is amplified with larger blow fraction values; notice that, to the left of the peak, the performance parameters are the lowest for the highest value of F_B .

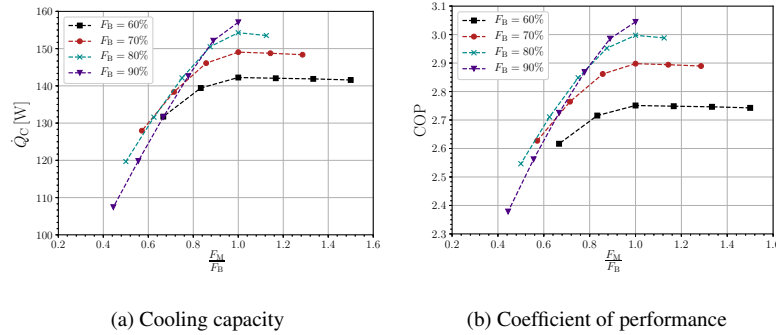


Fig. 14: Performance of the AMR system for various blow and magnetization fractions, utilization of 0.4 and and high magnetic field of 1.3 T

The influence of the utilization is demonstrated in Figure 15, where the cooling capacity is plotted for different utilization factors. For increasing Φ in this range, not only do the overall values of cooling capacity increase, but also the importance of choosing the blow fraction becomes clearer. In these ranges of utilization and blow fraction, the cooling capacity increases because the higher transfer rate associated with higher flow rates dominates over the loss of regenerator effectiveness.

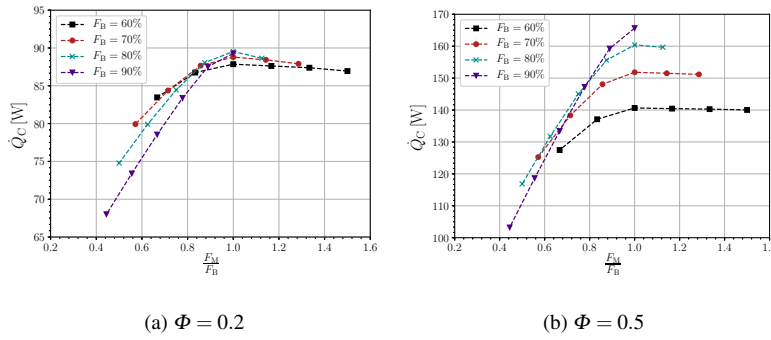


Fig. 15: Influence of utilization on the cooling capacity of the AMR system for various blow and magnetization fractions, with high magnetic field of 1.3 T

The above results can be evaluated from another point of view with Figure 16, where the coefficient of performance is plotted as contour levels. This type of map is useful because, since B_{\min} and τ are fixed, each point in this graph completely characterizes a magnetic ramp profile, and each subplot with fixed Φ and F_B characterizes the fluid flow profile. As expected, the performance increases for the higher values both B_{\max} and F_M , where the magnetic ramp profile tends to the instantaneous magnetic profile with a large amplitude. Confirming the previous trends, the results are less sensitive to the magnetization fraction when $F_M \geq F_B$.

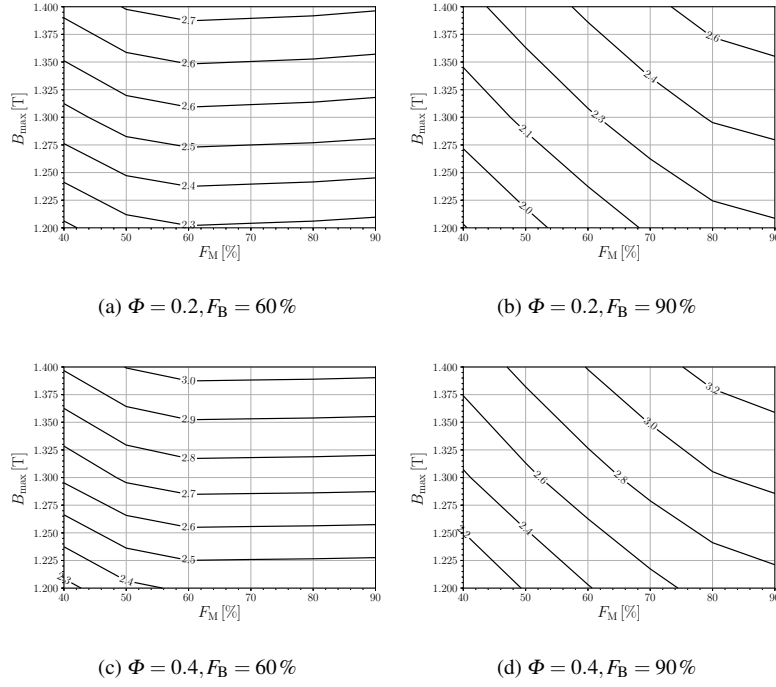


Fig. 16: Influence of utilization and blow fraction on the coefficient of performance of the AMR system for varying high magnetic field and magnetization fraction

3.2.2 Geometric analysis of the regenerators using the magnetic ramp profile

All previous results assumed a fixed regenerator geometry, with the goal of identifying the optimal fluid and magnetic profile parameters. It became clear that the magnetization fraction should be as large as possible, but that raises some challenges in realizing abrupt changes in the magnetic field. The value of $F_M = 70\%$ is then chosen as a compromise, with a corresponding $F_B = F_M$. The mean value of the utilization factor of $\Phi = 0.4$ is also chosen as reference in the next results.

Figure 17 shows the cooling capacity, coefficient of performance and second-law efficiency for varying magnetic field and regenerator height. As expected, larger regenerators

can produce the desired performance with lower magnetic fields. It can also be seen that this configuration for an AMR system can achieve values of η_{2nd} compatible with conventional vapor compression systems [42, 43], although these numerical results do not include mechanical losses.

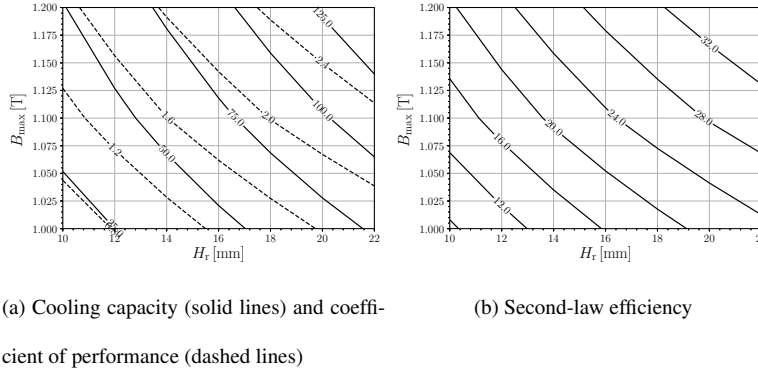


Fig. 17: Performance of the AMR with varying regenerator height and high magnetic field, with fixed $F_M = F_B = 70\%$ and $\Phi = 0.4$

4 Conclusions

To the authors' knowledge, this is the first study where magnetic and fluid flow profiles for an AMR model are mathematically modeled and the model parameters are changed in an integrated and systematic way. The instantaneous (square wave), rectified cosine and ramp magnetic profiles were implemented in an AMR model, together with an instantaneous fluid flow profile, and the profile parameters were varied simultaneously with the regenerator geometric parameters. These waveforms can be found in existing MR devices published in the literature. A valve model was also incorporated into a more realistic computation of the coefficient of performance.

When comparing the instantaneous and the rectified [cosine](#) magnetic profiles, the cooling capacity associated with the former can be almost 200 % higher than with the latter, for the same utilization and average high magnetic field and considering optimal blow fractions. The rectified [cosine](#) profile suffers from high values of the low magnetic field, and reduction of blow fraction up to the minimum tested value of 60 % is not enough to overcome the loss in cooling capacity resulting from this effect.

An analysis of power contributions showed that the cost of the higher cooling capacity for the instantaneous profile is a higher valve power associated with the longer blow duration, dominating the other contributions. However, the coefficient of performance is still higher for the square wave. Hence, even though sinusoidal waveforms can be obtained with more compact systems, step-like variations of high amplitude of the magnetic field are preferred if performance is more critical.

The ramp magnetic profile is a feasible approximation for the instantaneous profile without abrupt changes in the magnetic field plateaus. For an AMR device operating with this profile and the instantaneous fluid flow profile, both cooling capacity and coefficient of performance are maximized if the blow duration is equal to the period of constant magnetic field; if this exact synchronization is not possible, making the magnetization plateau wider than the flow plateau results in a smaller reduction of the performance metrics than [in the case where the magnetization plateau](#) is narrower.

With this strategy and using average values of utilization, it is possible to achieve second-law efficiency levels compatible with [those of](#) vapor-compression systems. Hence the ramp magnetic profile is identified as a suitable target profile in the design of magnetic circuits for AMR devices.

Conflict of Interest Statement

There is no actual or potential conflict of interest including any financial, personal or other relationships with other people or organizations that could inappropriately influence, or be perceived to influence, the present work.

Acknowledgements This work was funded by the INCT (National Institutes of Science and Technology) Program (CNPq Grant no. 443696/2014-4; FAPESC Grant no.2018TR1576). Additional funding was provided by CAPES (Talents for Innovation Program - Grant No. 88887.194773/2018-00) to F. Fortkamp and J. Lozano. Financial support from EMBRAPPII, Embraco and CODEMGE is also acknowledged.

References

1. P. Bansal, E. Vineyard, and O. Abdelaziz. Status of not-in-kind refrigeration technologies for household space conditioning, water heating and food refrigeration. *International Journal of Sustainable Built Environment*, 1:85–101, 2012.
2. IIR. 36th informatory note on refrigeration technologies: Flammable refrigerants. Available at http://www.iifir.org/userfiles/file/publications/notes/NoteTech_36_EN_nkyix2fcj7.pdf, 2017. Accessed on October 30th, 2018.
3. S. Lionte, M. Risser, C. Vasile, L. Elouad, and C. Muller. Adapting an active magnetic regenerator to a continuous fluid flow application. *International Journal of Refrigeration*, 85:303–313, 2018.
4. A. Smith, C. R. H. Bahl, R. Björk, K. Engelbrecht, K. K. Nielsen, and N. Pryds. Materials challenges for high performance magnetocaloric refrigeration devices. *Advanced Energy Materials*, 2:1288–1318, 2012.
5. A. Kitanovski, U. Plaznik, J. Tušek, and A. Poredoš. New thermodynamic cycles for magnetic refrigeration. *International Journal of Refrigeration*, 37:28–35, 2014.
6. R. Gimaev, Y. Spichkin, B. Kovalev, K. Kamilov, V. Zverev, and A. Tishin. Review on magnetic refrigeration devices based on HTSC materials. *International Journal of Refrigeration*, 100:1–12, 2019.
7. A. Greco, C. Aprea, A. Maiorino, and C. Masselli. A review of the state of the art of solid-state caloric cooling processes at room-temperature before 2019. *International Journal of Refrigeration*, 106:66 –

- 88, 2019.
8. A. Kitanovski. Energy applications of magnetocaloric materials. *Advanced Energy Materials*, 10: 1903741, 2020.
 9. G. H. Kaneko, A. C. Souza, F. Moro, F. C. Colman, W. A. S. Conceição, C. S. Alves, and P. V. Trevizoli. Design and assembling of a magnetic circuit for a thermomagnetic motor apparatus. *Journal of the Brazilian Society of Mechanical Sciences and Engineering*, 41:394, 2019.
 10. R. Teyber, P. V. Trevizoli, I. Niknia, T. V. Christiaanse, P. Govindappa, and A. Rowe. Experimental performance investigation of an active magnetic regenerator subject to different fluid flow waveforms. *International Journal of Refrigeration*, 74:38–46, 2017.
 11. A. T. D. Nakashima, S. L. Dutra, P. V. Trevizoli, and J. R. Barbosa, Jr. Influence of the flow rate waveform and mass imbalance on the performance of active magnetic regenerators. Part I: Experimental analysis. *International Journal of Refrigeration*, 93:236–248, 2018.
 12. F. P. Fortkamp, D. Eriksen, K. Engelbrecht, C. R. H. Bahl, J. A. Lozano, and J. R. Barbosa, Jr. Experimental investigation of different fluid flow profiles in a rotary multi-bed active magnetic regenerator device. *International Journal of Refrigeration*, 91:46–54, 2018.
 13. P. O. Cardoso, M. C. Destro, M. G. Alvarez, J. A. Lozano, J. R. Barbosa, Jr., and V. J. De Negri. Transient model and energy assessment of a digital solenoid valve system for a magnetic refrigerator. In *Proceedings of the 16th Brazilian Congress of Thermal Sciences and Engineering*, Vitória, 2016.
 14. P. O. Cardoso. An electrovalve system for hydraulic management of active magnetic regenerators, 2018. Master's Thesis (Mechanical Engineering), Federal University of Santa Catarina (in Portuguese).
 15. A. T. D. Nakashima, S. L. Dutra, G. Hoffmann, J. A. Lozano, and J. R. Barbosa, Jr. Performance assessment of solenoid valves as flow distributors for an active magnetic regenerator. In *Proceedings of the 8th International Conference on Caloric Cooling (Thermag VIII)*, Darmstadt, Germany, 2018.
 16. G. Hoffmann, S. L. Dutra, P. O. Cardoso, A. T. D. Nakashima, J. A. Lozano, and J. R. Barbosa, Jr. Actuation and control of electric valves for a magnetic refrigerator. In *Proceedings of the 24th ABCM International Congress of Mechanical Engineering (COBEM 2017)*, Curitiba, Brazil, 2017.
 17. R. Bjørk and K. Engelbrecht. The influence of the magnetic field on the performance of an active magnetic regenerator (AMR). *International Journal of Refrigeration*, 34:192–203, 2011.
 18. M. A. Benedict, S. A. Sherif, D. G. Beers, and M. G. Schroeder. Design and performance of a novel magnetocaloric heat pump. *Science and Technology for the Built Environment*, 22(5):520–526, 2016.

19. U. Plaznik, J. Tušek, A. Kitanovski, and A. Poredoš. Numerical and experimental analyses of different magnetic thermodynamic cycles with an active magnetic regenerator. *Applied Thermal Engineering*, 59: 52–59, 2013.
20. P. V. Trevizoli, J. R. Barbosa, Jr., A. Tura, D. Arnold, and A. Rowe. Modeling of thermomagnetic phenomena in active magnetocaloric regenerators. *Journal of Thermal Science and Engineering Applications*, 6:031016, 2014.
21. S. Oh, S. Min, and J.-P. Hong. Air gap flux density waveform design of surface-mounted permanent magnet motor considering magnet shape and magnetization direction. *IEEE Transactions on Magnetics*, 49(5):2393–2396, 2013.
22. I. Park and S. Jeong. Development of the active magnetic regenerative refrigerator operating between 77 K and 20 K with the conduction cooled high temperature superconducting magnet. *Cryogenics*, 88: 106–115, 2017.
23. P. V. Trevizoli, T. V. Christiaan, P. Govindappa, I. Niknia, R. Teyber, J. R. Barbosa, Jr., and A. Rowe. Magnetic heat pumps: An overview of design principles and challenges. *Science and Technology for the Built Environment*, 22(5):507–519, 2016.
24. F. P. Fortkamp, J. A. Lozano, and J.R. Barbosa, Jr. Analytical solution of concentric two-pole Halbach cylinders as a preliminary design tool for magnetic refrigeration systems. *Journal of Magnetism and Magnetic Materials*, 444:87 – 97, 2017.
25. F. P. Fortkamp, G. B. Lang, J. A. Lozano, and J. R. Barbosa, Jr. Design trade-offs for an active magnetic regenerator device. *Applied Thermal Engineering*, 165:114467, 2020.
26. A. M. Momen, O. Abdelaziz, K. Gluesenkamp, E. Vineyard, and M. Benedict. Thermofluid analysis of magnetocaloric refrigeration. In *Proceedings of the ASME 2014 International Mechanical Engineering Congress and Exposition*, Montreal, Canada, November 2014.
27. M. Zhang, O. Abdelaziz, A. M. Momen, and A. Abu-Heiba. A numerical analysis of a magnetocaloric refrigerator with a 16-layer regenerator. *Scientific Reports*, 7:13962, 2017.
28. H.R.E.H. Boucekara, A. Kedous-Lebouc, J.P. Yonnet, and C. Chillet. Multiobjective optimization of AMR systems. *International Journal of Refrigeration*, 37:63–71, 2014.
29. H. Ganjehsarabi, I. Dincer, and A. Gungor. Analysis and optimisation of a cascade active magnetic regenerative refrigeration system. *International Journal of Exergy*, 19:143–160, 2016.

30. S. Roy, S. Poncet, and M. Sorin. Sensitivity analysis and multiobjective optimization of a parallel-plate active magnetic regenerator using a genetic algorithm. *International Journal of Refrigeration*, 75:276–285, 2017.
31. R. Teyber, P.V. Trevizoli, T. V. Christiaanse, P. Govindappa, I. Niknia, and A. Rowe. Permanent magnet design for magnetic heat pumps using total cost minimization. *Journal of Magnetism and Magnetic Materials*, 442:87–96, 2017.
32. P. V. Trevizoli, A. T. Nakashima, and J. R. Barbosa, Jr. Performance evaluation of an active magnetic regenerator for cooling applications – part II: Mathematical modeling and thermal losses. *International Journal of Refrigeration*, 72:206–217, 2016.
33. D. A. Nield and A. Bejan. *Convection in Porous Media*. Springer, New York, 3 edition, 2006.
34. D. Eriksen, K. Engelbrecht, C. R. H. Bahl, R. Bjørk, and K. K. Nielsen. Effects of flow balancing on active magnetic regenerator performance. *Applied Thermal Engineering*, 103:1–8, 2016.
35. K. K. Nielsen, J. Tusek, K. Engelbrecht, S. Schopfer, A. Kitanovski, C. R. H. Bahl, A. Smith, N. Pryds, and A. Poredos. Review on numerical modeling of active magnetic regenerators for room-temperature applications. *International Journal of Refrigeration*, 34:603–616, 2011.
36. C. R. H. Bahl and K. K. Nielsen. The effect of demagnetization on the magnetocaloric properties of gadolinium. *Journal of Applied Physics*, 105:013916, 2009.
37. S. A. Klein. EES — Engineering Equation Solver, Professional Version v9.339. F-Chart Software, 2013. Available at <http://fchart.com>.
38. T. Lei, K. Engelbrecht, K. K. Nielsen, and C. T. Veje. Study of geometries of active magnetic regenerators for room temperature magnetocaloric refrigeration. *Applied Thermal Engineering*, 111:1232–1243, 2017.
39. I. Niknia, O. Campbell, T. V. Christiaanse, P. Govindappa, R. Teyber, P. V. Trevizoli, and A. Rowe. Impacts of configuration losses on active magnetic regenerator device performance. *Applied Thermal Engineering*, 106:601 – 612, 2016.
40. G. F. Peixer, J. A. Lozano, and J. R. Barbosa, Jr. Performance evaluation of AMRs using different casings. Book of Abstracts for the Danish Days on Caloric Materials and Devices, 2017.
41. H. Neves Bez, A. T. D. Nakashima, G. B. Lang, J. A. Lozano, and J. R. Barbosa, Jr. Numerical simulations and experimental tests of Gd-Y multi-layered active magnetic regenerators. In *Proceedings of the Eighth IIR Conference on Caloric Cooling (Thermag VIII)*, Darmstadt (Germany), 2018.

-
42. C. J. L. Hermes and C. Melo. A first-principles simulation model for the start-up and cycling transients of household refrigerators. *International Journal of Refrigeration*, 31(8):1341 – 1357, 2008.
 43. C. O. R. Negrão and C. J. L. Hermes. Energy and cost savings in household refrigerating appliances: A simulation-based design approach. *Applied Energy*, 88(9):3051 – 3060, 2011.